

Facile Fabrication of Ag Electrodes for CO<sub>2</sub>-to-CO Conversion with Near-Unity Selectivity and High Mass Activity

*Original*

Facile Fabrication of Ag Electrodes for CO<sub>2</sub>-to-CO Conversion with Near-Unity Selectivity and High Mass Activity / Monti, Nicolò B. D.; Fontana, Marco; Sacco, Adriano; Chiodoni, ANGELICA MONICA; Lamberti, Andrea; Pirri, Candido F.; Zeng, Juqin. - In: ACS APPLIED ENERGY MATERIALS. - ISSN 2574-0962. - ELETTRONICO. - 5:12(2022), pp. 14779-14788. [10.1021/acsaem.2c02143]

*Availability:*

This version is available at: 11583/2974735 since: 2023-01-17T17:41:12Z

*Publisher:*

AMER CHEMICAL SOC

*Published*

DOI:10.1021/acsaem.2c02143

*Terms of use:*

This article is made available under terms and conditions as specified in the corresponding bibliographic description in the repository

*Publisher copyright*

(Article begins on next page)

# Facile Fabrication of Ag Electrodes for CO<sub>2</sub>-to-CO Conversion with Near-Unity Selectivity and High Mass Activity

Nicolò B. D. Monti, Marco Fontana, Adriano Sacco, Angelica Chiodoni, Andrea Lamberti, Candido F. Pirri, and Juqin Zeng\*



Cite This: *ACS Appl. Energy Mater.* 2022, 5, 14779–14788



Read Online

ACCESS |



Metrics & More



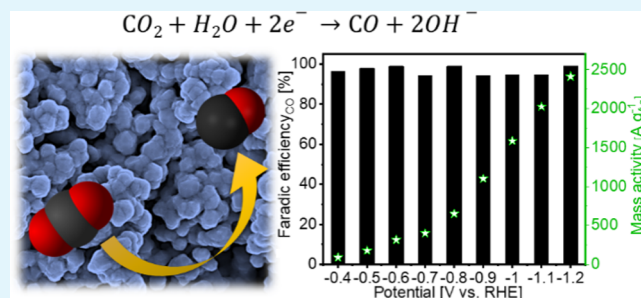
Article Recommendations



Supporting Information

**ABSTRACT:** Electrochemical reduction of CO<sub>2</sub> into valuable chemicals is considered a promising approach to achieve a carbon-neutral circular economy. This work aims at CO<sub>2</sub> conversion to CO with high efficiency at silver (Ag) electrodes with low catalyst loadings. The free-standing electrodes were simply prepared via sputtering deposition, achieving an easy control of the Ag loading. In CO<sub>2</sub> electrolysis, a relatively low Ag loading of 151.3 μg cm<sup>-2</sup> approaches 100% CO selectivity in both KHCO<sub>3</sub> and KOH electrolytes. In a KHCO<sub>3</sub> electrolyte, this electrode achieves current densities as high as 26.6 and 56.5 mA cm<sup>-2</sup> at -1.0 and -1.2 V vs reversible hydrogen electrode (RHE), respectively, corresponding to mass activities of 175.8 and 373.4 A g<sub>Ag</sub><sup>-1</sup>. Moreover, it also demonstrates high stability during a 15 h test at -1.2 V vs RHE, showing high retention in both the CO selectivity and geometric current density. By optimizing the operation conditions, a single-pass CO<sub>2</sub> to CO conversion of about 22% is achieved, and such a high value is maintained for 14 h. When changing to the KOH electrolyte, the electrode shows an impressive increase in current density, achieving 240.0 and 365.0 mA cm<sup>-2</sup> at -1.0 and -1.2 V vs RHE, respectively, corresponding to a high mass activity of 1586.3 and 2412.5 A g<sub>Ag</sub><sup>-1</sup>. In addition, excellent CO selectivity (>90%) is obtained in a wide potential range from -0.3 to -1.2 V vs RHE.

**KEYWORDS:** carbon dioxide, electrocatalysis, carbon monoxide, silver, mass activity, sputtering



## 1. INTRODUCTION

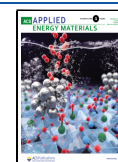
Electrochemical conversion of carbon dioxide (CO<sub>2</sub>) to value-added chemicals and fuels is of high interest from both economic and environmental perspectives since it can not only realize long-term storage of renewable electricity but also favor a sustainable carbon cycle and mitigate climate changes.<sup>1,2</sup> The electrochemical CO<sub>2</sub> reduction reaction (CO<sub>2</sub>RR) can result in a range of products, mainly including carbon monoxide (CO), formic acid (HCOOH), methane (CH<sub>4</sub>), ethylene (C<sub>2</sub>H<sub>4</sub>), ethanol (C<sub>2</sub>H<sub>5</sub>OH), and methanol (CH<sub>3</sub>OH). As a versatile C1-building block,<sup>3</sup> CO is considered the most important product and is intensively used in large industrial processes such as Fischer–Tropsch synthesis of hydrocarbons<sup>4</sup> and Monsanto/Cativa acetic acid synthesis.<sup>5</sup> Previous studies demonstrated that gold (Au),<sup>6,7</sup> silver (Ag),<sup>8,9</sup> zinc (Zn),<sup>10–12</sup> palladium (Pd),<sup>13</sup> some Cu-based materials,<sup>14–16</sup> and single-atom transition metals anchored in N-doped carbon (N–C–Me, Me = Co, Fe, Ni)<sup>17–19</sup> are selective for CO<sub>2</sub> reduction to CO. Among them, Au is considered the benchmark electrocatalyst for this purpose due to the highest activity and selectivity, while Ag is the most promising one for large-scale application since it is much more abundant and less expensive compared to Au. Many studies showed that the activity and CO selectivity of Ag catalysts can be further

improved by tuning morphology,<sup>20</sup> particle size,<sup>21</sup> and crystal facets<sup>22</sup> and by surface modification with oxygen,<sup>23</sup> halide anions,<sup>24</sup> and organic molecules.<sup>25</sup> The mechanism study of CO<sub>2</sub>RR on Ag electrode surfaces was also widely investigated by density functional theory calculations<sup>26</sup> and experimental observations,<sup>27,28</sup> showing that Ag dominantly produces CO, and it also has the potential to yield other molecules including C–C coupled products, depending on the surface geometric and electronic structures. Despite significant success on the catalyst development and reaction mechanism study, scarce studies were focused on the development of high-performance Ag electrodes through simple, fast, scalable, and low-cost methods. In the literatures, many free-standing Ag electrodes were fabricated by treating Ag foils,<sup>24,29</sup> Ag wires,<sup>30</sup> and Ag alloys,<sup>31</sup> and supported Ag electrodes were also prepared by coating powder-like catalysts onto a substrate such as glassy carbon,<sup>32</sup> carbon paper,<sup>23,33</sup> and polymeric membrane.<sup>34</sup> Most

Received: July 7, 2022

Accepted: November 7, 2022

Published: November 28, 2022



of them were tested in a batch cell at low current densities. Despite the scarce literatures, the critically important role of electrode development in the CO<sub>2</sub>RR was demonstrated. Sargent et al.<sup>35</sup> prepared Ag electrodes by sputtering a Ag catalyst on a PTFE membrane, followed by the coating of carbon nanoparticles. The resulting gas diffusion electrodes (GDEs) showed good CO<sub>2</sub>RR performance with a CO selectivity over 90% at current densities above 150 mA cm<sup>-2</sup> in a flow cell, while the mass activity of the Ag catalyst was not evaluated and PTFE substrates are expensive. Gascon et al.<sup>36</sup> studied carbon cloth-supported Ag GDEs, exhibiting high CO<sub>2</sub>RR efficiency with good CO selectivity (>96%), high current density (300 mA cm<sup>-2</sup>), and mass activity (1864 mA mg<sub>Ag</sub><sup>-1</sup>). Despite the good performance, these GDEs were fabricated by a tedious fabrication process starting from a layer-by-layer growth of a Ag coordination polymer onto a carbon-based microporous layer, followed by the electrodecomposition of the polymer.

In this work, we propose a novel and fast method to fabricate high surface area Ag GDEs in one single step. The nanostructured Ag thin layer was deposited onto a carbon paper by sputtering at room temperature and served as electrodes for CO<sub>2</sub>RR without any further treatments. Such a method provides easy control of the properties of the electrodes including Ag loading, morphology, purity, and reproducibility. The obtained electrodes were tested in a flow reactor with gas-fed CO<sub>2</sub>, which ensures high CO<sub>2</sub> diffusion rate and shortens the diffusion distance from the substrate to catalyst layer. CO<sub>2</sub>RR experiments show that the electrode with a relatively low loading of Ag can catalyze the CO<sub>2</sub>RR with high activity, excellent CO selectivity, and good stability. Particularly, the high mass activity of 2412.5 A g<sub>Ag</sub><sup>-1</sup> obtained on the sputtered Ag GDEs can remarkably reduce the employment of Ag metal, lowering the price of the electrode fabrication and increasing the sustainability.

## 2. EXPERIMENTAL SECTION

**2.1. Preparation of Ag Electrodes.** Sputtering (Quorum Technologies Ltd., Q150T) was used to prepare the Ag GDEs. A carbon paper (GDL; SIGRACET 28BC, Ion Power GmbH) was used as the substrate and a silver disk (99.99%, Testbourne) as the target. The carbon paper with a microporous layer and a certain amount of poly(tetrafluoroethylene) can enhance the gas diffusion and hence improve the behaviors of the electrodes in the gas-involved reactions.<sup>37–39</sup> The deposition method started with cleaning of the target to improve the quality of deposition. Two different deposition currents, namely, 30 and 50 mA, were applied, and the deposition time varied from 100 to 700 s, as shown in Table 1. The samples are denoted as AgXsYmA, where X and Y indicate the deposition time and current, respectively.

**2.2. Physical and Chemical Characterizations.** The morphology of the Ag electrodes was studied by means of field emission scanning electron microscopy (FESEM) with a Zeiss Auriga microscope.

X-ray diffraction (XRD) patterns of the samples were acquired with a PANalytical X'Pert Pro diffractometer (Cu K $\alpha$  radiation, 40 kV and 30 mA) equipped with an X'Celerator detector. The analysis of the whole XRD patterns with the Pawley method was carried out with MAUD software.<sup>40</sup> The cubic Ag structure (space group *Fm-3m*, ID: 1100136 in the Crystallography Open Database) was used for refinement. Line broadening due to the crystallite size was modeled with the size-strain model developed by Popa.<sup>41</sup> No significant contribution to line broadening due to microstrain was revealed. The contribution to peak line shapes by the X-ray diffractometer was determined by previous refinement of the XRD pattern of the LaB6 NIST standard sample measured in identical conditions. The

**Table 1. Samples Prepared with Sputtering**

sample	deposition current [mA]	deposition time [s]	Ag loading <sup>a</sup> [ $\mu\text{g cm}^{-2}$ ]
Ag200s30mA	30	200	131.5
Ag300s30mA	30	300	173.4
Ag500s30mA	30	500	282.1
Ag700s30mA	30	700	381.5
Ag100s50mA	50	100	73.9
Ag200s50mA	50	200	151.3
Ag300s50mA	50	300	282.7
Ag500s50mA	50	500	473.0

<sup>a</sup>Ag loading is calculated by weighting the GDL before and after deposition.

contribution to the XRD data by the GDL substrate was considered as background by importing in MAUD an XRD pattern of the pristine GDL.

**2.3. Electrochemical Tests and Product Analyses.** Electrochemical impedance spectroscopy (EIS) measurements were performed in a three-electrode single-compartment cell at room temperature with a Metrohm Autolab electrochemical workstation. The working electrode was an Ag electrode with a geometric area of 0.2 cm<sup>2</sup>. A Pt wire was used as the counter electrode and Ag/AgCl (3 M Cl<sup>-</sup>) as the reference. The electrolyte was a CO<sub>2</sub>-saturated 2.0 M KHCO<sub>3</sub> (potassium bicarbonate, 99.7%, Sigma-Aldrich) aqueous solution. EIS measurements were performed at various potentials of -0.6, -0.8, -1.0, and -1.2 V vs reversible hydrogen electrode (RHE) with an AC signal of 10 mV of amplitude and 10<sup>-2</sup>–10<sup>5</sup> Hz frequency range. Unless otherwise specified, all potentials refer to RHE.

The CO<sub>2</sub>RR experiments were conducted in a custom-made three-compartment flow cell, as illustrated in Scheme S1. An ion exchange membrane was used to separate the cathodic and anodic sides. The cathodic side was divided into two compartments by the working electrode that is a free-standing Ag electrode with a geometric area of 1.5 cm<sup>2</sup>. A mini Ag/AgCl (1 mm, leak-free LF-1) was used as the reference electrode and inserted in the catholyte. A Pt foil (Goodfellow, 99.95%) was used as the counter electrode and immersed in the anolyte. In the case of a KHCO<sub>3</sub> electrolyte, a cation exchange membrane (Nafion Membrane N117) was used. Both catholyte and anolyte were 25 mL of 2.0 M KHCO<sub>3</sub> aqueous solution and were circulated at 2 mL min<sup>-1</sup> during the test. Constant CO<sub>2</sub> flows of 10 and 25 mL min<sup>-1</sup> were maintained at anodic and cathodic compartments, respectively. When a KOH electrolyte was used, an anion exchange membrane (Sustainion 37-50, Dioxide materials) was employed. Both catholyte and anolyte were 1.0 M KOH solution and passed through the compartments at 2 mL min<sup>-1</sup> during the test. A constant CO<sub>2</sub> flow of 25 mL min<sup>-1</sup> was maintained for the gas compartment to supply the reactant. The reported potentials were corrected by compensating 85% of the ohmic drop (iR-compensation). Electrode potentials after iR-compensation were rescaled to the RHE reference by applying the Nernst equation,  $E_{\text{vsRHE}} = E_{\text{vsAg/AgCl}} + E_{\text{Ag/AgCl (3M Cl}^-)} + 0.0591 \times \text{pH}$ .

Gas-phase products were analyzed on-line by a microgas chromatograph ( $\mu\text{GC}$ , Fusion, INFICON), which is composed of two channels with a 10 m Rt-Molsieve 5A column and an 8 m Rt-Q-Bond column, respectively, and each channel with a microthermal conductivity detector. The inlet of  $\mu\text{GC}$  was connected to the cathodic side of the electrochemical cell, as shown in Scheme S1. The faradic efficiency (FE) for each gas-phase product was determined from its concentration in the outlet gas stream, as shown in eq 1

$$\text{FE} = \frac{V \times t \times C \times n \times F}{V_m \times Q} \quad (1)$$

where  $V_m$  is the molar volume of an ideal gas (L mol<sup>-1</sup>),  $V$  is the flow rate of CO<sub>2</sub> at the cathodic side (L min<sup>-1</sup>),  $t$  is the electrolysis time (min),  $Q$  is the total charge passed through the system during the electrolysis time  $t$  (coulombs),  $C$  is the concentration of the gas

product (% v/v),  $n$  is the number of electrons required to obtain one molecule of this product ( $n = 2$  for CO and H<sub>2</sub> formation), and  $F$  is the Faraday constant (96 485 C mol<sup>-1</sup>).

The partial current density of CO production is calculated via multiplying the geometric current density by its faradic efficiency, according to eq 2

$$j_{\text{CO}} = j_{\text{geo}} \times FE_{\text{CO}}$$

### 3. RESULTS AND DISCUSSION

**3.1. Characterizations of Ag Electrodes.** The deposition parameters determine the catalyst loading, as summarized in Figure 1 and Table 1. A higher deposition current results in a

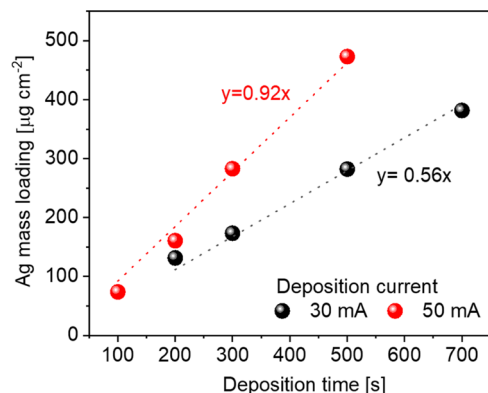


**Figure 1.** Ag mass loadings of electrodes prepared at different currents for different deposition times. The dotted lines shall guide the eye.

larger catalyst loading when the deposition time is fixed, and a longer deposition time leads to a higher catalyst loading at each deposition current. The Ag loading proportionally increases as lengthening the deposition time and the increase rate is higher at a higher deposition current.

FESEM analysis has been performed to study the morphology of the Ag electrodes. For all considered deposition parameters, porous Ag films are obtained, homogeneously covering the underlying GDL (Figures S1 and S2). The electrodes deposited at 30 mA show a similar top view, except that the particle aggregations slightly increase in size with extending the deposition time, as shown in Figure 2a–d. The morphology of the electrodes prepared at 50 mA exhibits a similar trend, showing no significant dependence on the deposition time except the particle size (Figure 2e,f).

The crystalline structure of the Ag electrodes has been analyzed by XRD. All of the samples share similar patterns (Figure 3a), showing only the peaks associated with the Ag cubic phase and contributions from the GDL substrate. As increasing the deposition time, these peaks increase in intensity relative to the background and GDL contribution at each current with Ag(111) clearly shown in Figure 3b. This outcome indicates that the weight percentage of Ag increases with increasing the deposition time for each current parameter, consistent with the results shown in Figure 1 and Table 1.

Further insight into the structure of the different Ag electrodes is provided by the Pawley refinement of XRD data. Table 2 provides refined values for the lattice constant and crystallite size obtained from the whole pattern fitting shown in Figures S3 and S4. Regarding the 30 mA series of samples, there is no significant effect of the deposition time on the lattice constant, while there is a general increase in crystallite size. Similar outcomes are also revealed in the 50 mA series of samples. Moreover, it is found that the crystalline size is bigger for the 50 mA sample than the 30 mA one with a similar mass loading (Figure S5).

**3.2. Comparison of Various Ag Electrodes.** Chronoamperometric tests were performed to study the activity and selectivity of the electrodes. CO and H<sub>2</sub> are the main gaseous products in each test, and negligible amounts of HCOOH were detected in the catholyte in some tests. In general, all samples

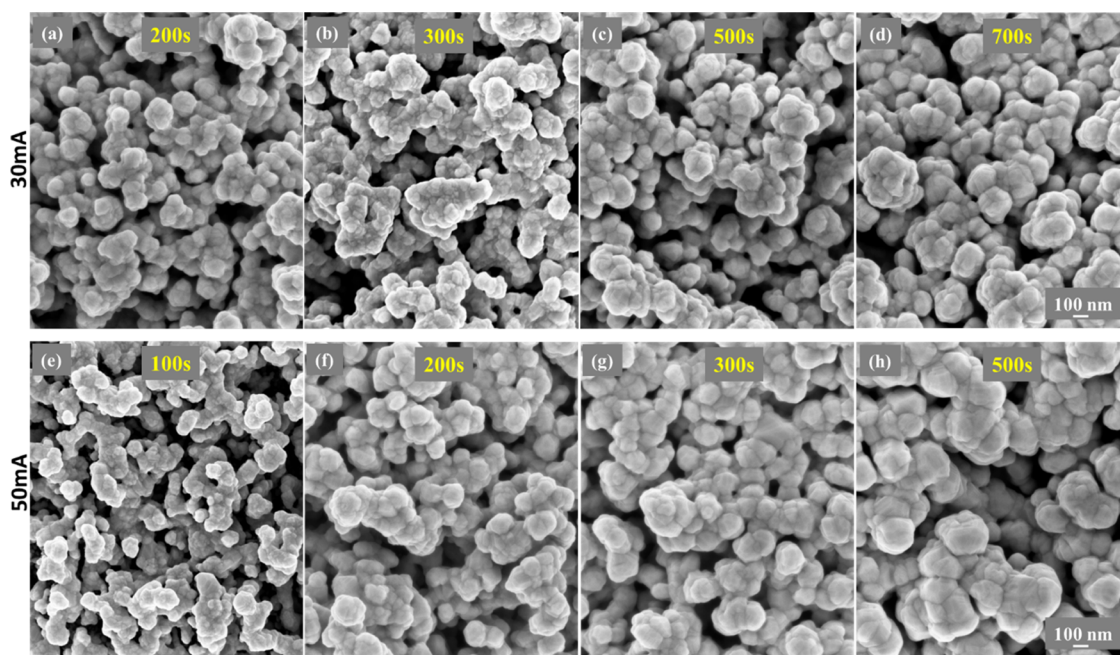


**Figure 2.** FESEM images of electrodes prepared at 30 mA with different deposition times: (a) 200 s, (b) 300 s, (c) 500 s, and (d) 700 s and electrodes prepared at 50 mA with different deposition times: (e) 100 s, (f) 200 s, (g) 300 s, and (h) 500 s.

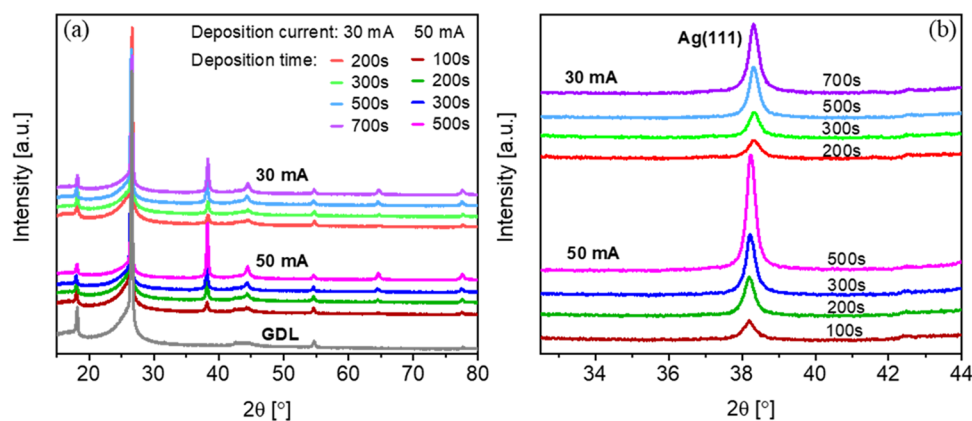


Figure 3. XRD patterns of all Ag electrodes in (a) long range and in short range (b).

Table 2. Pawley Refined Lattice Constant “a” and Crystallite Size Values for Different Ag Electrodes (Uncertainties Reported in Brackets)

sample	a (Å)	size (Å)
Ag200s30mA	4.086 (±2)	153 (±4)
Ag300s30mA	4.087 (±2)	199 (±5)
Ag500s30mA	4.087 (±1)	236 (±3)
Ag700s30mA	4.088 (±1)	219 (±3)
Ag100s50mA	4.091 (±2)	167 (±5)
Ag200s50mA	4.088 (±1)	218 (±4)
Ag300s50mA	4.085 (±1)	269 (±5)
Ag500s50mA	4.087 (±1)	279 (±3)

show a similar trend; that is, the current density and CO selectivity increase as raising the overpotential. However, the performance of the samples exhibits some distinct differences, as shown in Figures 4 and 5.

Figure 4 compares the electrodes prepared at 30 mA with different deposition durations at various investigated potentials. The Ag200s30mA sample with the lowest catalyst loading ( $131.5 \mu\text{g cm}^{-2}$ ) displays average performance at all potentials, showing a CO selectivity of 16, 48, and 64% at  $-0.8$ ,  $-1.0$ , and

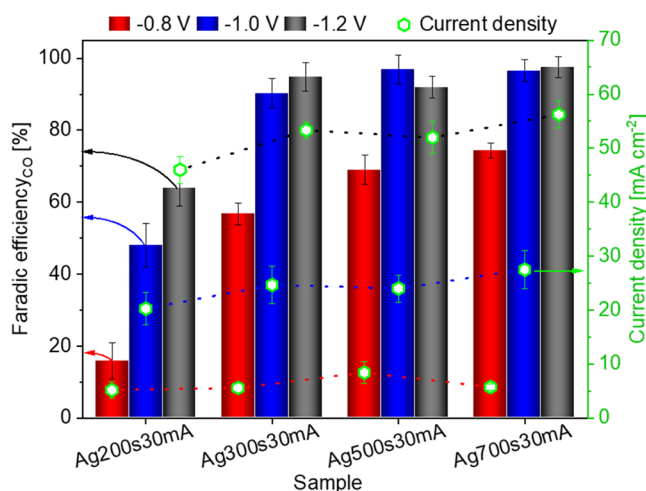


Figure 4. CO selectivity (bars, left axis) and geometric current densities (hexagons, right axis) at different potentials on the samples prepared at 30 mA. The dotted lines shall guide the eye (current densities: at  $-0.8$  V, red line;  $-1.0$  V, blue line; and  $-1.2$  V, black line).

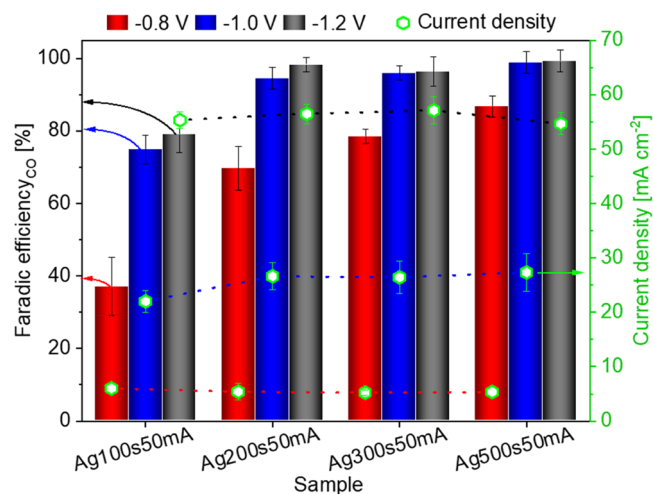
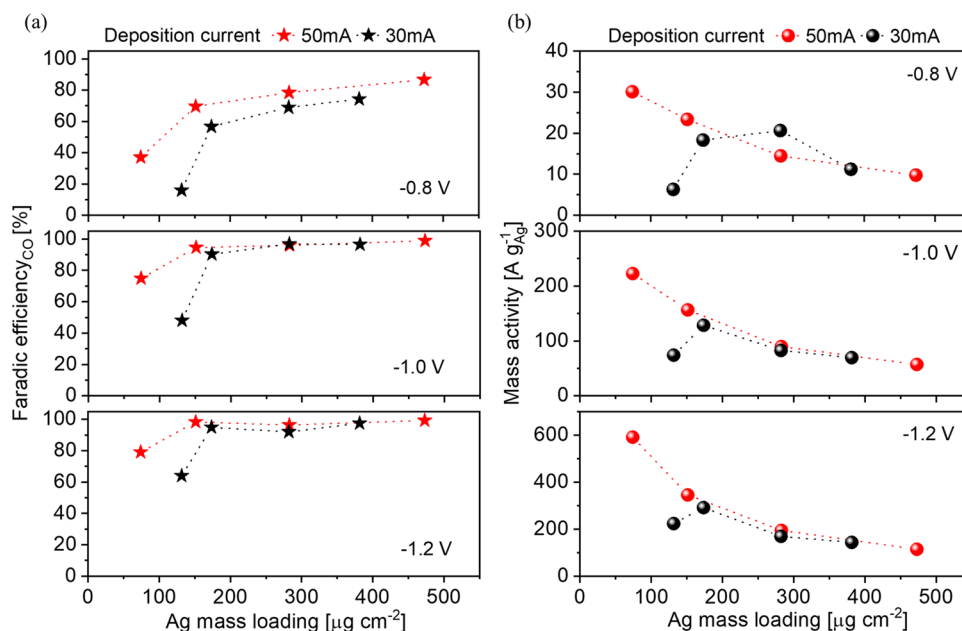


Figure 5. CO selectivity (bars, left axis) and geometric current densities (hexagons, right axis) at different potentials on the samples prepared at 50 mA. The dotted lines shall guide the eye (current densities: at  $-0.8$  V, red line;  $-1.0$  V, blue line; and  $-1.2$  V, black line).

$-1.2$  V, respectively. A clear increase in CO selectivity as increasing the Ag loading is observed at  $-0.8$  V, and such enhancement is less significant at more negative potentials when the Ag loading is higher than  $131.5 \mu\text{g cm}^{-2}$ . All samples with higher Ag loadings ( $>131.5 \mu\text{g cm}^{-2}$ ) perform similarly and show an excellent CO selectivity ( $>90\%$ ) at both  $-1.0$  and  $-1.2$  V. The sum of FE values for CO and  $\text{H}_2$  (Figure S6) reach around 100%, indicating that no significant amounts of other products are formed. In contrast to the selectivity, the current density is similar among different samples at  $-0.8$  V, while it generally increases with increasing the Ag loading at both  $-1.0$  and  $-1.2$  V. At  $-0.8$  V, the current densities are below  $10 \text{ mA cm}^{-2}$ , and they range from 20 to  $27 \text{ mA cm}^{-2}$  at  $-1.0$  V and from 46 to  $56 \text{ mA cm}^{-2}$  at  $-1.2$  V.

The comparison of the samples prepared at 50 mA is shown in Figure 5. Similarly, the CO selectivity and current density increase as raising the overpotential on each sample. It is interesting to note that the Ag300s50mA and Ag500s50mA samples achieve good FE<sub>CO</sub> values ( $>80\%$ ) at  $-0.8$  V and excellent ones ( $>90\%$ ) at more negative potentials. Nearly unity conversion of  $\text{CO}_2$  to CO is achieved at  $-1.0$  and  $-1.2$  V on the samples with higher Ag loadings ( $\geq 151.3 \mu\text{g cm}^{-2}$ ), and the HER is almost suppressed (Figure S7). All samples show a



**Figure 6.** Comparison of the samples at different potentials: (a) CO selectivity and (b) mass activity. The dotted lines shall guide the eye.

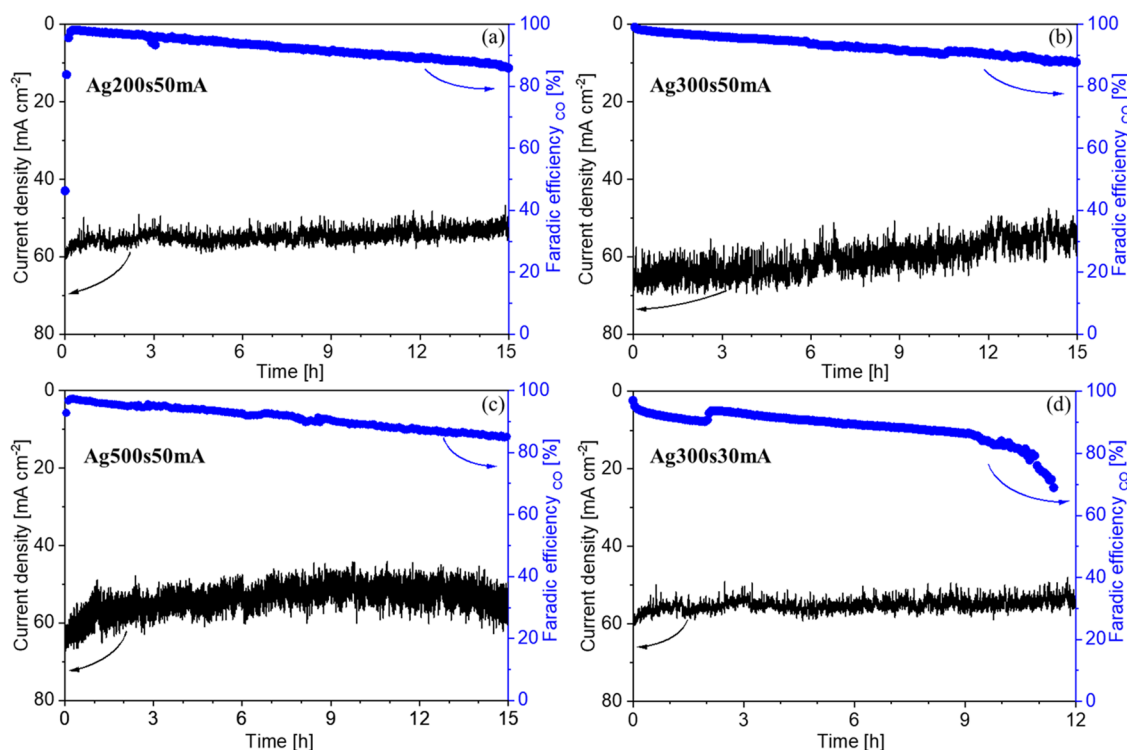


**Figure 7.** Long-term tests: CO faradic efficiency and geometric current density as a function of time on (a) Ag200s50mA, (b) Ag300s50mA, (c) Ag500s50mA, and (d) Ag300s30mA.

similar current density at  $-0.8$  V, which is between 5 and 6 mA cm<sup>-2</sup>. A current density ranging from 22 to 27 mA cm<sup>-2</sup> is achieved at  $-1.0$  V, and a current density between 55 and 57 mA cm<sup>-2</sup> is found on the electrodes at  $-1.2$  V. It is clear that the electrodes prepared at the deposition currents of 30 and 50 mA achieve a similar range of current density at each potential.

The present work aims to minimize the catalyst loading and maximize the exploitation of Ag simultaneously obtaining good CO<sub>2</sub>RR performance. To evaluate this aspect, the mass activity is calculated through dividing the CO partial current density by

the Ag mass loading. Figure 6 compares the FE<sub>CO</sub> and mass activity of all samples at various potentials. As shown in Figure 6a, the sample prepared at 50 mA shows slightly higher FE<sub>CO</sub> compared with that prepared at 30 mA with a similar Ag loading, especially at  $-0.8$  V. At  $-1.0$  and  $-1.2$  V, good CO selectivity (>90%) is achieved on the electrodes with Ag loadings higher than 150 μg cm<sup>-2</sup>, independent of the deposition current. Similarly, the mass activity of the electrode is also highly relevant to the Ag loading, but it is almost independent on the deposition current when the Ag loading is

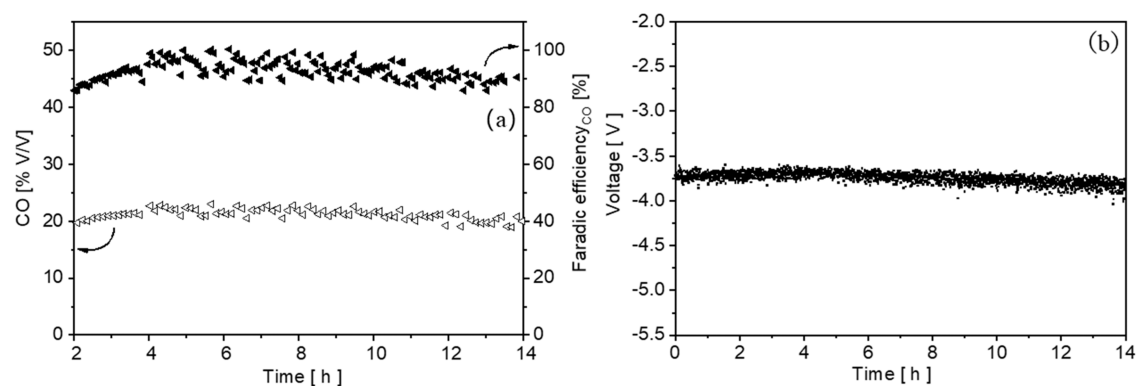


**Figure 8.** Long-term test on a Ag200s50mA electrode in the two-electrode mode: (a) CO percentage (%V/V) in the vent gas and CO faradic efficiency and (b) cell voltage as a function of time.

higher than  $150 \mu\text{g cm}^{-2}$ , as shown in Figure 6b. Generally, it decreases as the catalyst loading increases, especially at low Ag loadings.

The specific activity of all electrodes was also compared to evaluate their intrinsic activity for the  $\text{CO}_2\text{RR}$  to CO. To evaluate this aspect, the  $j_{\text{CO}}$  must be normalized by the electrochemically active surface area (ECSA). Since the ECSA is considered to be proportionally associated to the double-layer capacitance  $C_{\text{dl}}$ , the intrinsic activity of various materials can be compared by investigating the  $C_{\text{dl}}$ -normalized current densities. Through EIS analysis (see the Supporting Information and Figure S8 for details), the  $C_{\text{dl}}$  value is found to be 1.6, 1.1, 1.0, and 1.4  $\text{mF cm}^{-2}$  for Ag200s30mA, Ag300s30mA, Ag500s30mA, and Ag700s30mA, respectively, and 1.1, 0.7, 0.6, and 0.6  $\text{mF cm}^{-2}$  for Ag100s50mA, Ag200s50mA, Ag300s50mA, and Ag500s50mA, respectively. As shown in Figure S9, the electrode prepared at 50 mA shows higher activity compared with the one fabricated at 30 mA with a similar Ag loading at each potential. Both sets of electrodes prepared at 30 and 50 mA exhibit a similar dependence on the Ag mass loading at all potentials. The activity significantly increases with increasing the Ag loading until  $150 \mu\text{g cm}^{-2}$ . A further rise in the Ag loading leads to a much slower increase in the activity for the electrodes prepared at 50 mA and even a decrease for those prepared at 30 mA. It is worthy to notice that this trend is similar to that of the charge transfer time constant  $\tau$  calculated as the product of  $C_{\text{dl}}$  and the charge transfer resistance  $R_{\text{ct}}$  obtained by EIS analysis<sup>42</sup> and reported in Figure S10. This result suggests that the electrode activity is dominated by the charge transfer process. Given that  $\tau$  values already take into account the ECSA (through  $C_{\text{dl}}$ ), it appears that the increase of Ag loading makes the charge transfer related to the single catalytic site faster until a certain extent is reached, and then, it slows down.<sup>43</sup> This outcome may deserve further study, possibly involving time-resolved spectroscopy techniques. Overall, by comparing the selectivity, mass activity, and specific activity, it is possible to state that the optimal samples possess a Ag loading of about  $150 \mu\text{g cm}^{-2}$ , resulting in excellent  $\text{FE}_{\text{CO}}$  values and good mass activities of about 175.8 and 373.4  $\text{A g}_{\text{Ag}}^{-1}$  at  $-1.0 \text{ V}$  and  $-1.2 \text{ V}$ , respectively, for the electrode deposited at 50 mA.

Long-term tests were performed at  $-1.2 \text{ V}$  on the optimal electrodes, namely, Ag200s50mA, Ag300s50mA, Ag500s50mA, and Ag300s30mA. Figure 7 shows the  $\text{FE}_{\text{CO}}$  and geometric current density as a function of time on various electrodes. As can be seen in Figure 7a, the Ag200s50mA sample shows an

initial  $\text{FE}_{\text{CO}}$  approaching 100% and a current density of about  $55 \text{ mA cm}^{-2}$ . During a 15 h test, the  $\text{FE}_{\text{CO}}$  and current density gradually decrease to 91% and  $53 \text{ mA cm}^{-2}$ , respectively. Despite the drop, the retention of the CO selectivity and current density is higher than 90%, demonstrating the good stability of this electrode. The Ag300s50mA and Ag500s50mA samples show similar stability with respect to the Ag200s50mA, as displayed in Figures 7b,c. In contrast, the Ag300s30mA sample shows an excellent initial  $\text{FE}_{\text{CO}}$ , which quickly decreases after 10 h (Figure 7d). Despite the good retention in current density, the Ag300s30mA electrode is considered less stable compared to other samples.

**3.3. Study of an Optimal Ag Electrode.** The Ag200s50mA electrode was further tested in a two-electrode mode with a galvanostatic technique with an Ir-coated Ti plate (Ir-MMO, ElectroCell Europe A/S) as the anode (active area:  $10 \text{ cm}^2$ ) and a Ag GDE as the cathode (active area:  $6.2 \text{ cm}^2$ ). As shown in Figure 8b, the cell voltage maintains an almost stable value of about 3.7 V at a constant current density of  $45 \text{ mA cm}^{-2}$ . Figure 8a shows the CO% (%V/V) obtained in the vent gas and the  $\text{FE}_{\text{CO}}$  as a function of time. The CO selectivity has good retention and exhibits a gradual decrease in  $\text{FE}_{\text{CO}}$  from nearly 100% at the beginning to about 90% at the end of the test. The CO% maintains a quasi-constant value of about 22%, which is relatively high with respect to those reported in the literature.<sup>44–46</sup> The CO percentage in the vent gas represents the single-pass conversion of  $\text{CO}_2$ ; that is, it is the percentage of  $\text{CO}_2$  converted in a single run without gas circulation. Like the selectivity for a specific product, the single-pass conversion of  $\text{CO}_2$  is critical for minimizing the separation requirements and thus reducing both capital and operational costs. Moreover, when CO is the only gaseous product, the vent gas (a mixture of CO and  $\text{CO}_2$ ) can be further electrochemically reduced without any separation, allowing effective synthesis of  $\text{C}_{2+}$  products.<sup>47</sup> This two-step method is an up-to-date and encouraging technology for converting  $\text{CO}_2$  to highly valuable chemicals and fuels.<sup>48,49</sup> Hence, the high  $\text{CO}_2$ -to-CO single-pass conversion on the Ag electrode highlights the significance of our work.

The Ag200s50mA electrode is also investigated in the KOH electrolyte. The KOH electrolyte possesses enhanced conductivity with respect to  $\text{KHCO}_3$  one, resulting in higher reaction rates. Some studies also showed that surface hydroxyls offer effective sites to boost  $\text{CO}_2$  adsorption via the hydrogen bond, enhancing the  $\text{CO}_2\text{RR}$  activity and selectivity.<sup>50</sup> As seen from Figure 9a, the CO selectivity achieves an excellent value

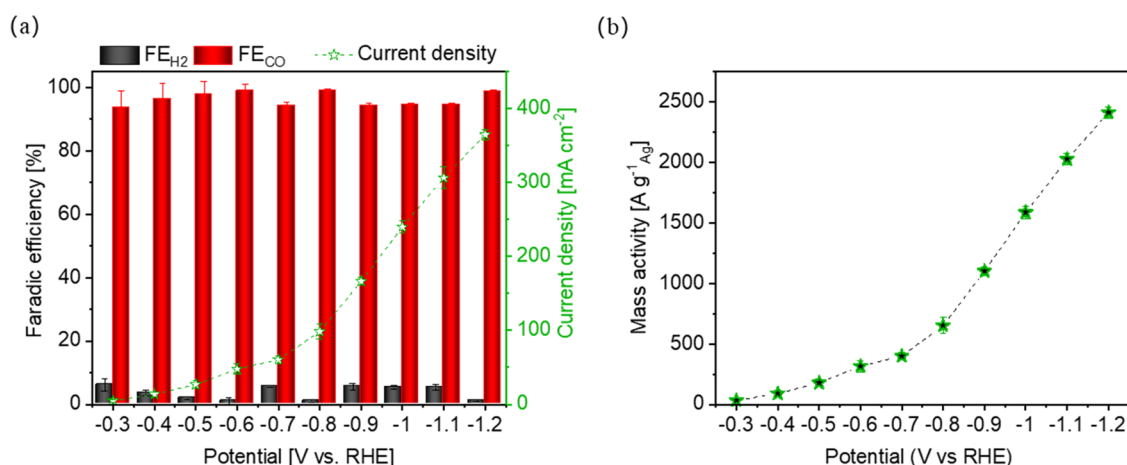


**Figure 9.**  $\text{CO}_2\text{RR}$  in 1.0 M KOH on Ag200s50mA: (a) CO and  $\text{H}_2$  selectivity and current density and (b) mass activity. The dotted lines shall guide the eye.

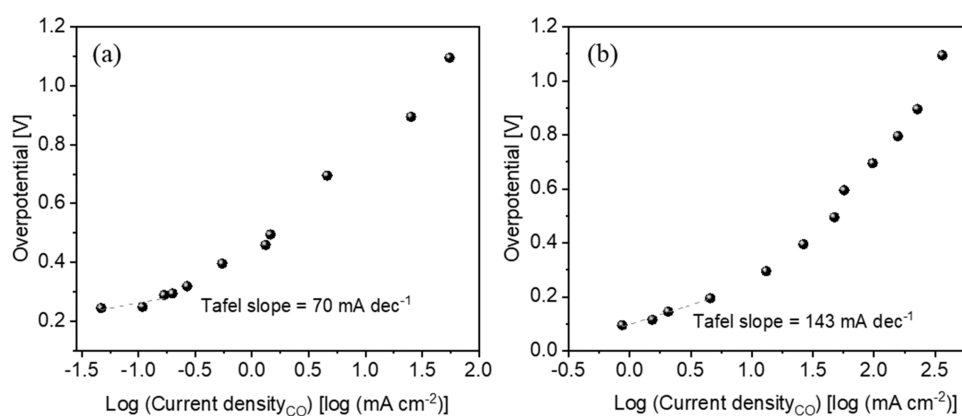


**Figure 10.** Tafel analysis has been performed on Ag200s50mA electrodes in both (a) 2.0 M  $\text{KHCO}_3$  and (b) 1.0 M KOH.

of 90% at  $-0.3 \text{ V}$ , and it approaches 100% at higher overpotentials. The current density is dramatically enhanced with respect to that obtained in  $\text{KHCO}_3$  electrolyte at the same potential. In particular, industrially relevant current densities of 240.0 and 365.0  $\text{mA cm}^{-2}$  are reached at  $-1.0$  and  $-1.2 \text{ V}$ , respectively, corresponding to high mass activities of 1586.3 and 2412.5  $\text{A g}_{\text{Ag}}^{-1}$  (Figure 9b). These outcomes demonstrate that the herein proposed Ag electrode outperforms most of the reported Ag-based materials and is in line with the best results in the literature (Table S1).<sup>51–55</sup> A long-term test has been performed on a Ag200s50mA electrode at  $-1.2 \text{ V}$  in 1.0 M KOH. As shown in Figure S11, the initial current density is 365  $\text{mA cm}^{-2}$  and gradually decreases to 285  $\text{mA cm}^{-2}$  after 6.5 h of test. The initial FE approaches 100% and then degrades with time, reaching 85% after 6.5 h. Compared to the stability at a lower current density in 2.0 M  $\text{KHCO}_3$ , the stability at a higher current density in 1.0 M KOH is much worse. This outcome is in agreement with the literature, which reports that the stability of the  $\text{CO}_2\text{RR}$  declines quickly with raising the current density.<sup>56</sup>

**3.4. Characterizations of Postmortem Electrodes and Discussion on the Reaction Mechanism.** FESEM and XRD analyses were performed on the tested Ag200s50mA electrodes. As shown in Figure S12, no significant changes are observed in the morphology of Ag electrodes after tests in  $\text{KHCO}_3$  and KOH electrolytes. XRD analysis shows that metallic Ag remains on the carbon paper substrate and no

secondary Ag-containing phases are present (Figure S13). Hence, instead of the restructuring of the Ag catalyst, the degradation of the  $\text{CO}_2\text{RR}$  performance during the long-term tests could be mainly attributed to the flooding and the formation of salts on the gas diffusion side of the GDE since significant amount of salt crystals and water was observed on the backside of the postmortem electrodes after long-term tests.

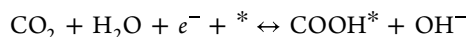
Tafel analysis is a vital tool for studying the mechanism of multistep reactions even though it has some limitations.<sup>57</sup> To reveal the rate-determining step (RDS) of the  $\text{CO}_2\text{RR}$  to CO, Tafel analysis has been performed on Ag200s50mA electrodes in both 2.0 M  $\text{KHCO}_3$  and 1.0 M KOH electrolytes. As shown in Figure 10, the Tafel plot is built by plotting the overpotential as a function of CO partial current density ( $j_{\text{CO}}$ ) in the logarithm scale. Tafel slopes of 70 and 143  $\text{mA dec}^{-1}$  are observed in  $\text{KHCO}_3$  and KOH, respectively. Different Tafel slopes can be related to distinct RDSs of the  $\text{CO}_2\text{RR}$ .<sup>57</sup>

Due to the relatively high alkalinity of both electrolytes, water is more likely to act as a proton source instead of hydronium ions, and the  $\text{CO}_2\text{RR}$  proceeds through proton-coupled electron transfer (PCET) or decoupled proton transfer (PT)/electron transfer (ET) pathways.<sup>58,59</sup>

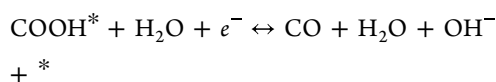
#### 1. First proton-coupled electron transfer



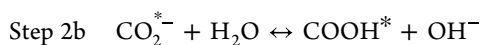
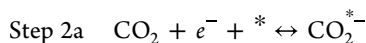
Step 1a



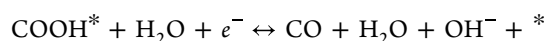
Step 1b



2. First decoupled proton/electron transfer



Step 2c



A Tafel slope of 70 mV dec<sup>-1</sup>, which is close to 56 mV dec<sup>-1</sup>, indicates a chemical step (e.g., PT) as the RDS, following a first PCET or ET. Hence, the RDS is likely to be step 1b or 2b in the KHCO<sub>3</sub> electrolyte. Differently, a slope of 143 mV dec<sup>-1</sup>, approximate to 120 mV dec<sup>-1</sup>, implies that the first PCET or ET is probably the RDS; that is, the step 1a or 2a is likely to be the RDS of the CO<sub>2</sub>RR to CO in KOH. It is noticed that the RDS varies in different electrolytes and the fundamental reasons behind it are not clear. It could be attributed to the combined effects of the intrinsic activity, the surface charge, and the mass transport,<sup>60</sup> and further investigations are needed to give concrete explanations.

#### 4. CONCLUSIONS

In this work, high-performance Ag electrodes have been fabricated via a simple and scaleable sputtering method for electrochemical conversion of CO<sub>2</sub> to CO. Nanostructured thin films of Ag are homogeneously formed on a carbon paper substrate and subsequently used as free-standing electrodes without any post-treatment. Such a fabrication method is simple, fast, and highly repeatable. The Ag electrodes show excellent selectivity and good activity for the CO<sub>2</sub> reduction to CO at low Ag loadings ≤150 μg cm<sup>-2</sup>, reaching approximately 100% CO selectivity and high mass activities of 1586.3 and 2412.5 A g<sub>Ag</sub><sup>-1</sup> at -1.0 and -1.2 V, respectively, outperforming most of reported Ag-based catalysts in the literature. In addition, the excellence is maintained on the Ag electrodes at a high single-pass CO<sub>2</sub> conversion of over 20% for 14 h. Based on these characteristics, the herein proposed Ag electrodes show good potential to be implemented in the industrial CO<sub>2</sub> conversion process, allowing to obtain a highly concentrated CO product at large scales and relatively low cost.

#### ■ ASSOCIATED CONTENT

##### SI Supporting Information

The Supporting Information is available free of charge at <https://pubs.acs.org/doi/10.1021/acsaem.2c02143>.

EIS analysis, a scheme of setups for CO<sub>2</sub> electrolysis, FESEM images of various Ag electrodes, XRD patterns and Pawley refinement (red line) of Ag electrodes, FE<sub>H2</sub> at different potentials on the samples prepared at 30 and 50 mA, specific activity of each electrode for the CO production at various potentials, comparison of the mass activity of Ag-based catalysts, representative Nyquist plot

of Ag electrodes and comparison of the charge transfer time constant, long-term test of Ag200s50mA at -1.2 V in 1.0 M KOH electrolyte, and postmortem XRD and FESEM analyses (PDF)

#### ■ AUTHOR INFORMATION

##### Corresponding Author

Juqin Zeng – Centre for Sustainable Future Technologies (CSFT), Istituto Italiano di Tecnologia - IIT, Turin 10144, Italy; [orcid.org/0000-0001-8885-020X](https://orcid.org/0000-0001-8885-020X); Phone: +39 011 2257719; Email: [Juqin.Zeng@iit.it](mailto:Juqin.Zeng@iit.it)

##### Authors

Nicolò B. D. Monti – Centre for Sustainable Future Technologies (CSFT), Istituto Italiano di Tecnologia - IIT, Turin 10144, Italy; Department of Applied Science and Technology (DISAT), Politecnico di Torino, Turin 10129, Italy

Marco Fontana – Department of Applied Science and Technology (DISAT), Politecnico di Torino, Turin 10129, Italy; Centre for Sustainable Future Technologies (CSFT), Istituto Italiano di Tecnologia - IIT, Turin 10144, Italy; [orcid.org/0000-0003-0894-2193](https://orcid.org/0000-0003-0894-2193)

Adriano Sacco – Centre for Sustainable Future Technologies (CSFT), Istituto Italiano di Tecnologia - IIT, Turin 10144, Italy; [orcid.org/0000-0002-9229-2113](https://orcid.org/0000-0002-9229-2113)

Angelica Chiodoni – Centre for Sustainable Future Technologies (CSFT), Istituto Italiano di Tecnologia - IIT, Turin 10144, Italy

Andrea Lamberti – Department of Applied Science and Technology (DISAT), Politecnico di Torino, Turin 10129, Italy; Centre for Sustainable Future Technologies (CSFT), Istituto Italiano di Tecnologia - IIT, Turin 10144, Italy; [orcid.org/0000-0003-4100-9661](https://orcid.org/0000-0003-4100-9661)

Candido F. Pirri – Centre for Sustainable Future Technologies (CSFT), Istituto Italiano di Tecnologia - IIT, Turin 10144, Italy; Department of Applied Science and Technology (DISAT), Politecnico di Torino, Turin 10129, Italy

Complete contact information is available at: <https://pubs.acs.org/doi/10.1021/acsaem.2c02143>

##### Author Contributions

N.M., M.F., A.S., and A.C. contributed to the investigations. A.L. contributed to the investigations and resources. C.P. contributed to the resources and supervision. J.Z. contributed to the investigations, supervision, and conceptualization. All authors contributed to the manuscript composition.

##### Funding

This research did not receive any specific grant from funding agencies in the public, commercial, or not-for-profit sectors.

##### Notes

The authors declare no competing financial interest. The authors declare that they have no known competing financial interests or personal relationships that could have appeared to influence the work reported in this paper.

#### ■ REFERENCES

- Costentin, C.; Robert, M.; Savéant, J. Catalysis of the Electrochemical Reduction of Carbon Dioxide. *Chem. Soc. Rev.* **2013**, *42*, 2423–2436.
- Appel, A. M.; Bercaw, J. E.; Bocarsly, A. B.; Dobbek, H.; DuBois, D. L.; Dupuis, M.; Ferry, J. G.; Fujita, E.; Hille, R.; Kenis, P.J.A.;

- Kerfeld, C. A.; Morris, R. H.; Peden, C.H.F.; Portis, A. R.; Ragsdale, S. W.; Rauchfuss, T. B.; Reek, J.N.H.; Seefeldt, L. C.; Thauer, R. K.; Waldrop, G. L. Frontiers, Opportunities, and Challenges in Biochemical and Chemical Catalysis of CO<sub>2</sub> Fixation. *Chem. Rev.* **2013**, *113*, 6621–6658.
- (3) Nielsen, D. U.; Hu, X. M.; Daasbjerg, K.; Skrydstrup, T. Chemically and Electrochemically Catalysed Conversion of CO<sub>2</sub> to CO with Follow-up Utilization to Value-Added Chemicals. *Nat. Catal.* **2018**, *1*, 244–254.
- (4) Dry, M. E. The Fischer-Tropsch Process: 1950-2000. *Catal. Today* **2002**, *71*, 227–241.
- (5) Jones, J. H. The Cativa™ Process for the Manufacture of Acetic Acid: Iridium Catalyst Improves Productivity in an Established Industrial Process. *Platinum Met. Rev.* **2000**, *44*, 94–105.
- (6) Liu, M.; Pang, Y.; Zhang, B.; De Luna, P.; Voznyy, O.; Xu, J.; Zheng, X.; Dinh, C. T.; Fan, F.; Cao, C.; Arquer, F.P.G.; Safaei, T. S.; Mepham, A.; Klinkova, A.; Kumacheva, E.; Filleter, T.; Sinton, D.; Kelley, S. O.; Sargent, E. H. Enhanced Electrocatalytic CO<sub>2</sub> Reduction via Field-Induced Reagent Concentration. *Nature* **2016**, *537*, 382–386.
- (7) Shaughnessy, C. I.; Sconyers, D. J.; Lee, H.-J.; Subramaniam, B.; Blakemore, J. D.; Leonard, K. C. Insights into Pressure Tunable Reaction Rates for Electrochemical Reduction of CO<sub>2</sub> in Organic Electrolytes. *Green Chem.* **2020**, *22*, 2434–2442.
- (8) Thevenon, A.; Rosas-Hernández, A.; Herreros, A.M.F.; Agapie, T.; Peters, J. C. *ACS Catal.* **2021**, *11*, 4530–4537.
- (9) Li, C.; Xiong, H.; He, M.; Xu, B.; Lu, Q. *ACS Catal.* **2021**, *11*, 12029–12037.
- (10) Zeng, J.; Rino, T.; Bejtka, K.; Castellino, M.; Sacco, A.; Farkhondehfar, M. A.; Chiodoni, A.; Drago, F.; Pirri, C. F. Coupled Copper-Zinc Catalysts for Electrochemical Reduction of Carbon Dioxide. *ChemSusChem* **2020**, *13*, 4128–4139.
- (11) Lourenço, M. A. O.; Zeng, J.; Jagdale, P.; Castellino, M.; Sacco, A.; Farkhondehfar, M. A.; Pirri, C. F. Biochar/Zinc Oxide Composites as Effective Catalysts for Electrochemical CO<sub>2</sub> Reduction. *ACS Sustainable Chem. Eng.* **2021**, *9*, 5445–5453.
- (12) Zeng, J.; Fontana, M.; Sacco, A.; Sassone, D.; Pirri, C. F. A study of the effect of electrode composition on the electrochemical reduction of CO<sub>2</sub>. *Catal. Today* **2022**, 397–399, 463–474.
- (13) Hoang, V. C.; Gomes, V. G.; Kornienko, N. Metal-based nanomaterials for efficient CO<sub>2</sub> electroreduction: Recent advances in mechanism, material design and selectivity. *Nano Energy* **2020**, *78*, 105311. Article number
- (14) Dong, W. J.; Lim, J. W.; Hong, D. M.; Park, J. Y.; Cho, W. S.; Baek, S.; Yoo, C. J.; Kim, W.; Lee, J.-L. Evidence of Local Corrosion of Bimetallic Cu–Sn Catalysts and Its Effects on the Selectivity of Electrochemical CO<sub>2</sub> Reduction. *ACS Appl. Energy Mater.* **2020**, *3*, 10568–10577.
- (15) Zeng, J.; Bejtka, K.; Di Martino, G.; Sacco, A.; Castellino, M.; Re Fiorentin, M.; Risplendi, F.; Farkhondehfar, M. A.; Hernández, S.; Cicero, G.; Pirri, C. F.; Chiodoni, A. Microwave-Assisted Synthesis of Copper-Based Electrocatalysts for Converting Carbon Dioxide to Tunable Syngas. *ChemElectroChem* **2020**, *7*, 229–238.
- (16) Sacco, A.; Speranza, R.; Savino, U.; Zeng, J.; Farkhondehfar, M. A.; Lamberti, A.; Chiodoni, A.; Pirri, C. F. An Integrated Device for the Solar-Driven Electrochemical Conversion of CO<sub>2</sub> to CO. *ACS Sustainable Chem. Eng.* **2020**, *8*, 7563–7568.
- (17) Zhao, J.; Deng, J.; Han, J.; Imhanria, S.; Chen, K.; Wang, W. Effective Tunable Syngas Generation via CO<sub>2</sub> Reduction Reaction by Non-Precious Fe-N-C Electrocatalyst. *Chem. Eng. J.* **2020**, *389*, 124323–124330.
- (18) Möller, T.; Ju, W.; Bagger, A.; Wang, X.; Luo, F.; Ngo Thanh, T.; Varela, A. S.; Rossmeisl, J.; Strasser, P. Efficient CO<sub>2</sub> to CO Electrolysis on Solid Ni–N–C Catalysts at Industrial Current Densities. *Energy Environ. Sci.* **2019**, *12*, 640–647.
- (19) Zhang, J.; Cai, W.; Hu, F. X.; Yang, H.; Liu, B. Recent advances in single atom catalysts for the electrochemical carbon dioxide reduction reaction. *Chem. Sci.* **2021**, *12*, 6800–6819.
- (20) Liu, S.; Tao, H.; Zeng, L.; Liu, Q.; Xu, Z.; Liu, Q.; Luo, J.-L. Shape-Dependent Electrocatalytic Reduction of CO<sub>2</sub> to CO on Triangular Silver Nanoplates. *J. Am. Chem. Soc.* **2017**, *139*, 2160–2163.
- (21) Zhang, L.; Wang, Z.; Mehio, N.; Jin, X.; Dai, S. Thickness- and Particle-Size-Dependent Electrochemical Reduction of Carbon Dioxide on Thin-Layer Porous Silver Electrodes. *ChemSusChem* **2016**, *9*, 428–432.
- (22) Clark, E. L.; Ringe, S.; Tang, M.; Walton, A.; Hahn, C.; Jaramillo, T. F.; Chan, K.; Bell, A. T. Influence of Atomic Surface Structure on the Activity of Ag for the Electrochemical Reduction of CO<sub>2</sub> to CO. *ACS Catal.* **2019**, *9*, 4006–4014.
- (23) Ishida, M.; Kikkawa, S.; Hori, K.; Teramura, K.; Asakura, H.; Hosokawa, S.; Tanaka, T. Effect of Surface Reforming via O<sub>3</sub> Treatment on the Electrochemical CO<sub>2</sub> Reduction Activity of a Ag Cathode. *ACS Appl. Energy Mater.* **2020**, *3*, 6552–6560.
- (24) Hsieh, Y.-C.; Betancourt, L. E.; Senanayake, S. D.; Hu, E.; Zhang, Y.; Xu, W.; Polyansky, D. E. Modification of CO<sub>2</sub> Reduction Activity of Nanostructured Silver Electrocatalysts by Surface Halide Anions. *ACS Appl. Energy Mater.* **2019**, *2*, 102–109.
- (25) Koshy, D. M.; Akhade, S. A.; Shugar, A.; Abiose, K.; Shi, J.; Liang, S.; Oakdale, J. S.; Weitzner, S. E.; Varley, J. B.; Duoss, E. B.; Baker, S. E.; Hahn, C.; Bao, Z.; Jaramillo, T. F. Chemical Modifications of Ag Catalyst Surfaces with Imidazolium Ionomers Modulate H<sub>2</sub> Evolution Rates during Electrochemical CO<sub>2</sub> Reduction. *J. Am. Chem. Soc.* **2021**, *143*, 14712–14725.
- (26) Zhang, X.-G.; Jin, X.; Wu, D.-Y.; Tian, Z.-Q. Selective Electrocatalytic Mechanism of CO<sub>2</sub> Reduction Reaction to CO on Silver Electrodes: A Unique Reaction Intermediate. *J. Phys. Chem. C* **2018**, *122*, 25447–25455.
- (27) Firet, N. J.; Blommaert, M. A.; Burdyny, T.; Venugopal, A.; Bohra, D.; Longo, A.; Smith, W. A. Operando EXAFS study reveals presence of oxygen in oxide-derived silver catalysts for electrochemical CO<sub>2</sub> reduction. *J. Mater. Chem. A* **2019**, *7*, 2597–2607.
- (28) Hatsukade, T.; Kuhl, K. P.; Cave, E. R.; Abram, D. N.; Jaramillo, T. F. Insights into the electrocatalytic reduction of CO<sub>2</sub> on metallic silver surfaces. *Phys. Chem. Chem. Phys.* **2014**, *16*, 13814–13819.
- (29) Ma, M.; Liu, K.; Shen, J.; Kas, R.; Smith, W. A. In Situ Fabrication and Reactivation of Highly Selective and Stable Ag Catalysts for Electrochemical CO<sub>2</sub> Conversion. *ACS Energy Lett.* **2018**, *3*, 1301–1306.
- (30) Huang, J.-F.; Wu, Y.-C. Tunable Ag Micromorphologies Show High Activities for Electrochemical H<sub>2</sub> Evolution and CO<sub>2</sub> Electrochemical Reduction. *ACS Sustainable Chem. Eng.* **2019**, *7*, 6352–6359.
- (31) Lu, Q.; Rosen, J.; Zhou, Y.; Hutchings, G. S.; Kimmel, Y. C.; Chen, J. G.; Jiao, F. A selective and efficient electrocatalyst for carbon dioxide reduction. *Nat. Commun.* **2014**, *5*, No. 3242.
- (32) Qi, K.; Zhang, Y.; Li, J.; Charmette, C.; Ramonda, M.; Cui, X.; Wang, Y.; Zhang, Y.; Wu, H.; Wang, W.; Zhang, X.; Voiry, D. Enhancing the CO<sub>2</sub>-to-CO Conversion from 2D Silver Nanoprisms via Superstructure Assembly. *ACS Nano* **2021**, *15*, 7682–7693.
- (33) Fan, T. T.; Wu, Q. L.; Yang, Z.; Song, Y. P.; Zhang, J. G.; Huang, P. P.; Chen, Z.; Dong, Y. Y.; Fang, W. P.; Yi, X. D. Electrochemically Driven Formation of Sponge-Like Porous Silver Nanocubes toward Efficient CO<sub>2</sub> Electroreduction to CO. *ChemSusChem* **2020**, *13*, 2677–2683.
- (34) Xi, W.; Ma, R.; Wang, H.; Gao, Z.; Zhang, W.; Zhao, Y. Ultrathin Ag Nanowires Electrode for Electrochemical Syngas Production from Carbon Dioxide. *ACS Sustainable Chem. Eng.* **2018**, *6*, 7687–7694.
- (35) Dinh, C.-T.; Pelayo García de Arquer, F.; Sinton, D.; Sargent, E. H. High Rate, Selective, and Stable Electroreduction of CO<sub>2</sub> to CO in Basic and Neutral Media. *ACS Energy Lett.* **2018**, *3*, 2835–2840.
- (36) Wang, R.; Haspel, H.; Pustovarenko, A.; Dikhtiarenko, A.; Russkikh, A.; Shterk, G.; Osadchii, D.; Ould-Chikh, S.; Ma, M.; Smith, W. A.; Takane, K.; Kapteijn, F.; Gascon, J. Maximizing Ag Utilization in High-Rate CO<sub>2</sub> Electrochemical Reduction with a

Coordination Polymer-Mediated Gas Diffusion Electrode. *ACS Energy Lett.* **2019**, *4*, 2024–2031.

(37) Martinez Crespiera, S.; Amantia, D.; Knipping, E.; Aucher, C.; Aubouy, L.; Amici, J.; Zeng, J.; Francia, C.; Bodoardo, S. Electrospun Pd-doped mesoporous carbon nano fibres as catalysts for rechargeable Li-O<sub>2</sub> batteries. *RSC Adv.* **2016**, *6*, 57335–57345.

(38) Vankova, S.; Francia, C.; Amici, J.; Zeng, J.; Bodoardo, S.; Penazzi, N.; Collins, G.; Geaney, H.; O'Dwyer, C. Influence of Binders and Solvents on Stability of Ru/RuO<sub>x</sub> Nanoparticles on ITO Nanocrystals as Li-O<sub>2</sub> Battery Cathodes. *ChemSusChem* **2017**, *10*, 575–586.

(39) Zeng, J.; Nair, J. R.; Francia, C.; Bodoardo, S.; Penazzi, N. Aprotic Li-O<sub>2</sub> cells: Gas diffusion layer (GDL) as catalyst free cathode and tetraglyme/LiClO<sub>4</sub> as electrolyte. *Solid State Ionics* **2014**, *262*, 160–164.

(40) Ferrari, M.; Lutterotti, L. Method for the simultaneous determination of anisotropic residual stresses and texture by X-ray diffraction. *J. Appl. Phys.* **1994**, *76*, 7246.

(41) Popa, N. C. The (hkl) Dependence of Diffraction-Line Broadening Caused by Strain and Size for all Laue Groups in Rietveld Refinement. *J. Appl. Crystallogr.* **1998**, *31*, 176–180.

(42) Savino, U.; Sacco, A.; Bejtka, A.; Castellino, M.; Farkhondehfar, M. A.; Chiodoni, A.; Pirri, P.; Tresso, E. Well performing Fe-SnO<sub>2</sub> for CO<sub>2</sub> reduction to HCOOH. *Catal. Commun.* **2022**, *163*, 106412.

(43) Hernández, S.; Tortello, M.; Sacco, A.; Quaglio, M.; Meyer, T.; Bianco, S.; Saracco, G.; Pirri, F.; Tresso, E. New Transparent Laser-Drilled Fluorine-doped Tin Oxide covered Quartz Electrodes for Photo-Electrochemical Water Splitting. *Electrochim. Acta* **2014**, *131*, 184–194.

(44) Xing, Z.; Hu, L.; Ripatti, D. S.; Hu, X.; Feng, X. *Nat Commun.*, *12* (2021), Article number 136.

(45) Dinh, C.-T.; Burdyny, T.; Kibria, M. G.; Seifitokaldani, A.; Gabardo, C. M.; García de Arquer, F. P.; Kiani, A.; Edwards, J. P.; De Luna, P.; Bushuyev, O. S.; Zou, C.; Quintero-Bermudez, R.; Pang, Y.; Sinton, D.; Sargent, E. H. CO<sub>2</sub> electroreduction to ethylene via hydroxide mediated copper catalysis at an abrupt interface. *Science* **2018**, *360*, 783–787.

(46) Ma, S.; Sadakiyo, M.; Luo, R.; Heima, M.; Yamauchi, M.; Kenis, P.J.A. One-step electrosynthesis of ethylene and ethanol from CO<sub>2</sub> in an alkaline electrolyzer. *J. Power Sources* **2016**, *301*, 219–228.

(47) Wang, X.; de Araujo, J. F.; Ju, W.; Bagger, A.; Schmies, H.; Kuhl, S.; Rossmeisl, J.; Strasser, P. Mechanistic reaction pathways of enhanced ethylene yields during electroreduction of CO<sub>2</sub>-CO co-feeds on Cu and Cu-tandem electrocatalysts. *Nat. Nanotechnol.* **2019**, *14*, 1063–1070.

(48) Romero Cuellar, N. S.; Scherer, C.; Kackar, B.; Eisenreich, W.; Huber, C.; Wiesner-Fleischer, K.; Fleischer, M.; Hinrichsen, O. Two-step electrochemical reduction of CO<sub>2</sub> towards multi-carbon products at high current densities. *J CO<sub>2</sub> Util.* **2020**, *36*, 263–275.

(49) Sisler, J.; Khan, S.; Ip, A. H.; Schreiber, M. W.; Jaffer, S. A.; Bobicki, E. R.; Dinh, C.-T.; Sargent, E. H. Ethylene Electrosynthesis: A Comparative Techno-economic Analysis of Alkaline vs Membrane Electrode Assembly vs CO<sub>2</sub>-CO-C<sub>2</sub>H<sub>4</sub> Tandems. *ACS Energy Lett.* **2021**, *6*, 997–1002.

(50) Deng, W.; Zhang, L.; Li, L.; Chen, S.; Hu, C.; Zhao, Z.-J.; Wang, T.; Gong, J. Crucial Role of Surface Hydroxyls on the Activity and Stability in Electrochemical CO<sub>2</sub> Reduction. *J. Am. Chem. Soc.* **2019**, *141*, 2911–2915.

(51) Kim, C.; Jeon, H. S.; Eom, T.; Shincheon Jee, M.; Kim, H.; Friend, C. M.; Min, B. K.; Hwang, Y. J. Achieving Selective and Efficient Electrocatalytic Activity for CO<sub>2</sub> Reduction Using Immobilized Silver Nanoparticles. *J. Am. Chem. Soc.* **2015**, *137*, 13844–13850.

(52) Abeyweera, S. C.; Yu, J.; Perdew, J. P.; Yan, Q.; Sun, Y. Hierarchically 3D Porous Ag Nanostructures Derived from Silver Benzenethiolate Nanoboxes: Enabling CO<sub>2</sub> Reduction with a Near-Unity Selectivity and Mass-Specific Current Density over 500 A/g. *Nano Lett.* **2020**, *20*, 2806–2811.

(53) Ma, S.; Liu, J.; Sasaki, K.; Lyth, S. M.; Kenis, P.J.A. Carbon Foam Decorated with Silver Nanoparticles for Electrochemical CO<sub>2</sub> Conversion. *Energy Technol.* **2017**, *5*, 861–863.

(54) Verma, S.; Lu, X.; Ma, S.; Masel, R. I.; Kenis, P.J.A. The effect of electrolyte composition on the electroreduction of CO<sub>2</sub> to CO on Ag based gas diffusion electrodes. *Phys. Chem. Chem. Phys.* **2016**, *18*, 7075–7084.

(55) Ma, S.; Luo, R.; Gold, J. I.; Yu, A. Z.; Kimbc, B.; Kenis, P.J.A. Carbon nanotube containing Ag catalyst layers for efficient and selective reduction of carbon dioxide. *J. Mater. Chem. A* **2016**, *4*, 8573–8578.

(56) Yang, K.; Kas, R.; Smith, W. A.; Burdyny, T. Role of the Carbon-Based Gas Diffusion Layer on Flooding in a Gas Diffusion Electrode Cell for Electrochemical CO<sub>2</sub> Reduction. *ACS Energy Lett.* **2021**, *6*, 33–40.

(57) Dunwell, M.; Luc, W.; Yan, Y.; Jiao, F.; Xu, B. Understanding Surface-Mediated Electrochemical Reactions: CO<sub>2</sub> Reduction and Beyond. *ACS Catal.* **2018**, *8*, 8121–8129.

(58) Zeng, J.; Re Fiorentin, M.; Fontana, M.; Castellino, M.; Risplendi, F.; Sacco, A.; Cicero, G.; Farkhondehfar, M. A.; Drago, F.; Pirri, C. F. *Appl. Catal., B* **2022**, *306*, No. 121089. Article number

(59) Luan, C.; Shao, Y.; Lu, Q.; Gao, S.; Huang, K.; Wu, H.; Yao, K. High-Performance Carbon Dioxide Electrocatalytic Reduction by Easily Fabricated Large-Scale Silver Nanowire Arrays. *ACS Appl. Mater. Interfaces* **2018**, *10*, 17950–17956.

(60) Zhu, X.; Huang, J.; Eikerling, M. Electrochemical CO<sub>2</sub> Reduction at Silver from a Local Perspective. *ACS Catal.* **2021**, *11*, 14521–14532.

## Recommended by ACS

### Highly Selective and Durable CO Production via Effective Morphology and Surface Engineering of ZnO Electrocatalysts

Rohini Subhash Kanase, Soon Hyung Kang, *et al.*

NOVEMBER 09, 2022  
ACS APPLIED ENERGY MATERIALS

READ 

### Hydrophobic Electrode Design for CO<sub>2</sub> Electroreduction in a Microchannel Reactor

Jing Lin, Zhenmin Cheng, *et al.*

FEBRUARY 02, 2022  
ACS APPLIED MATERIALS & INTERFACES

READ 

### Boosting the Electroreduction of CO<sub>2</sub> to Ethanol via the Synergistic Effect of Cu-Ag Bimetallic Catalysts

Hehua Tang, Bo-Lin Lin, *et al.*

NOVEMBER 04, 2022  
ACS APPLIED ENERGY MATERIALS

READ 

### Use of Nanoscale Carbon Layers on Ag-Based Gas Diffusion Electrodes to Promote CO Production

Lien Pacquets, Tom Bruegelmans, *et al.*

MAY 19, 2022  
ACS APPLIED NANO MATERIALS

READ 

Get More Suggestions >